# Neutron capture cross sections for the weak *s* process in massive stars

M. Heil,* F. Käppeler, and E. Uberseder†
*Forschungszentrum Karlsruhe, Institut für Kernphysik, Postfach 3640, D-76021 Karlsruhe, Germany*

R. Gallino‡ and M. Pignatari§
*Dipartimento di Fisica Generale, Università di Torino, Via. P. Giuria 1, I-10125 Torino, Italy*

(Received 16 April 2007; revised manuscript received 28 November 2007; published 29 January 2008)

Neutron capture nucleosynthesis in massive stars plays an important role in galactic chemical evolution as well as for the analysis of abundance patterns in very old metal-poor halo stars. The so-called weak *s*-process component, which is responsible for most of the *s* abundances between Fe and Sr, turned out to be very sensitive to the stellar neutron capture cross sections in this mass region and, in particular, of isotopes near the seed distribution around Fe. Activation measurements in a quasistellar neutron spectrum corresponding to a thermal energy of $kT = 25$ keV have been carried out on $^{58}$Fe, $^{59}$Co, $^{64}$Ni, $^{63}$Cu, and $^{65}$Cu. By a series of repeated irradiations with different experimental conditions, uncertainties between 3.0% and 4.6% could be achieved, factors of 2 to 3 more accurate than previous data. Compared to previous measurements, severe discrepancies were found for $^{63,65}$Cu. The consequences of these results have been studied by detailed model calculations for convective core He burning and convective shell C burning in massive stars.

DOI: 10.1103/PhysRevC.77.015808 PACS number(s): 25.40.Lw, 26.20.−f, 27.40.+z, 27.50.+e

## I. INTRODUCTION

The phenomenology of the *s* process implies that the solar abundance distribution is composed of two parts, a *main* component, which is responsible for the mass region from Y to Bi, and a *weak* component, which contributes to the region from Fe to Sr. The main and weak component can be assigned to low mass stars with $1 \leqslant M/M_{\odot} \leqslant 3$ and to massive stars with $M \geqslant 8M_{\odot}$, respectively ($M_{\odot}$ stands for the mass of the sun). Accordingly, the galactic enrichment with *s*-process material starts with the lighter *s* elements, because massive stars evolve much quicker.

Stellar models for the main *s*-process component in the mass range $A \geqslant 90$ refer to helium shell burning in thermally pulsing low mass asymptotic giant branch (AGB) stars [1]. This scenario is characterized by the subsequent operation of two neutron sources during a series of helium shell flashes. First, the $^{13}$C$(\alpha, n)^{16}$O reaction occurs under radiative conditions during the intervals between convective He-shell burning episodes. While the $^{13}$C reaction provides most of the neutron exposure at low temperatures of $1 \times 10^8$ K ($kT \sim 8$ keV) and relatively low neutron densities ($n_n \leqslant 10^7$ cm$^{-3}$), the resulting abundances are modified by a second burst of neutrons from the $^{22}$Ne$(\alpha, n)^{25}$Mg reaction, which is marginally activated during the next convective instability, when a short neutron burst with peak densities of $n_n \geqslant 10^{10}$ cm$^{-3}$ is released at temperatures of $2.7 \times 10^8$ K ($kT \sim 23$ keV). Although this second neutron burst accounts only for a few percent of the total exposure, it is essential for adjusting the final abundance patterns of the *s*-process branchings.

The *s* process in massive stars with $M \geqslant 8M_{\odot}$ operates in two major evolutionary stages, first during convective core He burning and subsequently during convective shell carbon burning. Another non-negligible contribution to the final *s* yields may come from a partial tiny convective He burning shell at the outer border of the C shell, whose existence depends on the adopted stellar model [2,3]. Neutrons are mainly produced by the $^{22}$Ne$(\alpha, n)^{25}$Mg reaction in both cases, but at rather different temperatures and neutron densities. During core He burning, neutrons are produced near core He exhaustion at temperatures of $T = (2.5\text{–}3.5) \times 10^8$ K for about $10^4$ years with neutron densities $\lesssim 10^6$ cm$^{-3}$, whereas the higher temperatures of $T = (1.0\text{–}1.4) \times 10^9$ K during the subsequent carbon shell burning phase give rise to peak values of about $10^{12}$ cm$^{-3}$ [4–6].

In both *s*-process scenarios, the stellar $(n, \gamma)$ cross sections of the involved isotopes constitute the essential nuclear physics input, but with an important difference: The high neutron exposure during the main component is sufficient for establishing equilibrium in the reaction flow, resulting in the so-called local approximation

$$\langle \sigma \rangle N_s = \text{constant};$$

though limited to isotopes between magic neutron numbers, this relation implies that the emerging *s* abundances are inversely proportional to the stellar cross sections and that the uncertainty of a particular cross section affects only the abundance of that specific isotope. In contrast, the neutron exposure in massive stars is too small to achieve flow equilibrium, and this means that cross section uncertainties are not only influencing the abundance of that particular

*Present address: GSI Darmstadt, Planckstr. 1, D-64291 Darmstadt, Germany; M.Heil@gsi.de
†Present address: University of Notre Dame, Notre Dame, Indiana, USA.
‡Also at Centre for Stellar and Planetary Astrophysics, Monash University, Victoria 3800, Australia.
§Present address: Astrophysics Group, School of Physical and Geographical Sciences, Keele University, UK.

 

isotope but have a potentially strong propagating effect on the abundances of the subsequent isotopes involved in the $s$-process chain as well.

This propagation effect became apparent after it was clear that the large discrepancies found in the existing time-of-flight (TOF) data for the $^{62}$Ni$(n,\gamma)^{63}$Ni reaction by a factor of two [7] and computations made with different Maxwellian averaged cross section (MACS) choices showed the existence of an important bottle-neck effect for the $s$-process reaction flow. As a change in the neutron capture rate of a single nucleus can significantly impact the abundances of many subsequent isotopes in the reaction chain, the limited quality of stellar cross section below $A = 120$ bears serious consequences for the contributions of the weak $s$ process to galactic chemical evolution.

The nucleosynthesis yields of the weak component are also important for the $r$ process. Since the $s$-process abundances can be determined reliably on the basis of experimental $(n,\gamma)$ cross sections, the $r$ abundances are commonly inferred by subtracting the main and weak $s$-process components from the solar values:

$$N_r = N_\odot - N_s.$$

The $r$-process abundance distribution obtained in this way can be used to test $r$-process models and, in particular for comparison with observations of ultra metal-poor (UMP) stars in the galactic halo [8].

In the mass region of the weak $s$ process, however, stellar neutron capture cross sections are mostly not available with the required accuracy. Existing data suffer not only from large uncertainties of more than 10%, but discrepancies between measurements are often much larger than the quoted uncertainties [9]. Therefore, the cross sections of the following nuclei at the beginning of the $s$-process path, i.e., $^{58}$Fe, $^{59}$Co, $^{64}$Ni, $^{63}$Cu, and $^{65}$Cu, have been remeasured. These isotopes have in common that their MACSs were all determined more than 20 years ago and that they have relatively small cross sections of less than 100 mbarn. This last point is crucial, because isotopes with small cross sections are known to give rise to large propagation effects in the final abundance distribution. In Sec. II, experimental technique and measurements are described, Sec. III deals with data analysis and results, and the astrophysical implications are discussed in Sec. IV.

## II. MEASUREMENTS

### A. Experimental technique

The activation method represents a well established and accurate approach to determine MACSs at $kT = 25$ keV by producing a quasistellar neutron spectrum via the $^7$Li$(p,n)^7$Be reaction [10]. This method has been extensively used, mostly for measurements related to the main $s$-process component (for recent examples see Refs. [11–13]). In the present experiments, the proton beam with an energy of $E_p = 1912$ keV, 30 keV above the reaction threshold, was delivered by the Karlsruhe 3.7 MV Van de Graaff accelerator with typical intensities of 100$\mu$A. The neutron production target consisted of 30$\mu$m thick metallic Li layers evaporated onto water cooled copper backings. In this way, neutrons are kinematically collimated into a forward cone of 120° opening angle. Neutron moderation is avoided since cooling is achieved by lateral heat conduction to the water flow outside of this cone. Throughout the irradiations the neutron flux was continuously monitored and recorded in time steps of typically 60 s by means of a $^6$Li-glass detector at 1 m distance from the target. This information is important to account for fluctuations of the neutron yield in evaluating the fraction $f_b$ of the reaction products that decay already during the irradiations.

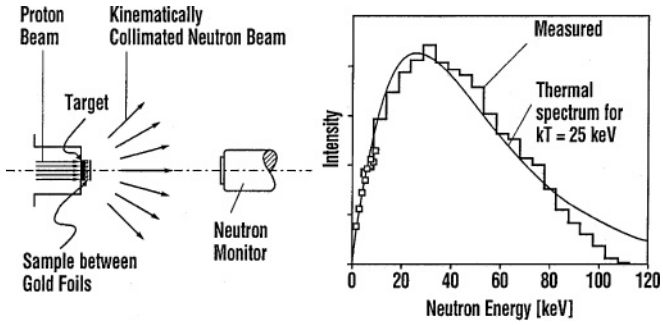


FIG. 1. Left: Schematic sketch of the activation setup. Right: The quasi-stellar neutron spectrum obtained with the $^7$Li$(p,n)^7$Be reaction (histogram and symbols) compared to a true Maxwell-Boltzmann distribution for a thermal energy of $kT = 25$ keV. Note that the experimental spectrum falls below the Maxwell-Boltzmann distribution above 80 keV and contains no neutrons above 106 keV.

A sketch of the experimental setup and a comparison of the resulting quasistellar neutron spectrum with a true Maxwell-Boltzmann distribution are shown in Fig. 1.

### B. Samples and irradiations

The samples were cut from metal foils of natural composition. As listed in Table I repeated activations were performed with samples that differed in diameter between 6 and 12 mm and in thickness between 0.03 and 0.5 mm. The samples

TABLE I. Samples and irradiation parameters.

| Activation | Sample[a] | Mass (mg) | Diameter (mm) | Irradiation time (min) | Integrated flux ($\times 10^{14}$) |
|---|---|---|---|---|---|
| 1 | Fe | 188.03 | 8 | 6929 | 6.791 |
| 2 | Fe | 421.65 | 12 | 6929 | 2.920 |
| 3 | Fe | 292.16 | 10 | 8499 | 7.999 |
| 4 | Co | 15.00 | 8 | 2879 | 1.528 |
| 5 | Co | 44.22 | 10 | 2871 | 2.485 |
| 6 | Ni | 277.72 | 8 | 415 | 0.8097 |
| 7 | Ni | 433.47 | 10 | 376 | 0.4097 |
| 8 | Ni | 401.63 | 12 | 400 | 0.3268 |
| 9 | Cu | 130.57 | 6 | 1071 | 2.181 |
| 10 | Cu | 232.07 | 8 | 1105 | 1.487 |
| 11 | Cu | 361.61 | 10 | 1397 | 1.028 |
| 12 | Cu | 130.8 | 6 | 15 | 0.05365 |
| 13 | Cu | 232.07 | 8 | 15 | 0.03605 |
| 14 | Cu | 361.61 | 10 | 15 | 0.02333 |

[a]All samples were cut from thin metal foils.

TABLE II. Decay properties of the product nuclei.

| Product nucleus | Half-life | $\gamma$-Ray energy (keV) | Intensity per decay (%) | Reference |
|---|---|---|---|---|
| $^{59}$Fe | $44.495 \pm 0.009$ d | 1099.25 | $56.5 \pm 1.8$ | [27] |
| $^{60}$Co | $5.2714 \pm 0.0005$ yr | 1173.23 | $99.85 \pm 0.03$ | [28] |
| | | 1332.49 | $99.9826 \pm 0.0006$ | |
| $^{65}$Ni | $2.5127 \pm 0.0003$ h | 1481.84 | $23.59 \pm 0.14$ | [29] |
| $^{64}$Cu | $12.700 \pm 0.002$ h | 1345.77 | $0.473 \pm 0.010$ | [30] |
| $^{66}$Cu | $5.120 \pm 0.014$ min | 1039.2 | $9.23 \pm 0.09$ | [31] |
| $^{198}$Au | $2.69517 \pm 0.00021$ d | 411.8 | $95.58 \pm 0.12$ | [32] |

were sandwiched between 0.03 mm thick gold foils for normalization to the well known gold reference cross section [14], and were placed completely inside the neutron cone, in direct contact with the neutron target at the position of highest flux.

Depending on the half-lives of the respective product nuclei, the irradiations lasted between 115 h in case of $^{58}$Fe and 15 min in case of $^{65}$Cu. The integrated neutron flux seen by the samples (last column of Table I) reflects the condition of the accelerator and the performance of the $^{7}$Li targets used and varies between a source strength of about $(0.7–3.0) \times 10^{9}$ s$^{-1}$. In total, 14 activations have been carried out for the determination of the five $(n, \gamma)$ cross sections of $^{58}$Fe, $^{59}$Co, $^{64}$Ni, $^{63}$Cu, and $^{65}$Cu.

### C. Induced activities

The induced activities are characterized by energetic $\gamma$-ray lines with well known relative intensities (Table II).

The $\gamma$-activities were counted by means of a shielded 76 cm$^3$ high purity Ge-detector (HPGe) with 1.7 keV resolution at 1.33 MeV $\gamma$-ray energy and a relative efficiency of 30%. Only two of the irradiated Ni samples (activations 6 and 7) were counted with a HPGe clover detector with a relative efficiency of 120%. This is the reason why activation 8 shows a much larger statistical uncertainty than was obtained in runs 6 and 7. Special adapters were used to ensure that the counting geometry was well defined and the positioning of the samples was reproducible within 0.1 mm. In all cases $\gamma$-ray backgrounds were small and had practically no effect on the uncertainty of the final cross section values. The excellent sensitivity of the experimental method is illustrated in Fig. 2 at the example of the $^{59}$Co$(n, \gamma)^{60}$Co reaction. In spite of the fact that the induced activities were low because of the long half-life of $^{60}$Co, the statistical uncertainties were much smaller than the respective systematic uncertainties (see below).

## III. RESULTS AND DISCUSSION

### A. Data analysis

The total number of activated nuclei $A$ is given by

$$A = \phi \cdot N \cdot \sigma \cdot f_b, \quad (1)$$

where $\phi$ is the time integrated neutron flux, $N$ the number of sample atoms, and $\sigma$ the spectrum averaged neutron capture cross section. The factor $f_b$ accounts for variations of the neutron flux and for the decay during activation.

The number of activated nuclei in Eq. (1) are determined from the number of counts in a characteristic $\gamma$-ray line,

$$C_\gamma = A \cdot K_\gamma \cdot \varepsilon_\gamma \cdot I_\gamma \cdot (1 - \exp(-\lambda t_m)) \cdot \exp(-\lambda t_w), \quad (2)$$

where $K_\gamma$ is a correction factor for $\gamma$-ray self-absorption, $\varepsilon_\gamma$ the efficiency of the HPGe-detector, $I_\gamma$ the line intensity, $t_w$ the waiting time between irradiation and counting, and $t_m$ the duration of the activity measurement. The time-integrated flux, $\phi$, is determined from the measured intensities of the 412 keV $\gamma$-ray line in the spectra of the two gold foils.

### B. Corrections and uncertainties

The experimental uncertainties are summarized in Table III, where the investigated reactions are indicated by the respective target nuclei.

Significant contributions to the overall uncertainty originate from the gold reference cross section, the efficiency of the HPGe detectors, and the time integrated neutron flux. The $^{58}$Fe and $^{63}$Cu cross sections are also affected by uncertain $\gamma$-decay intensities. Any improvement of these data would, therefore, be important.

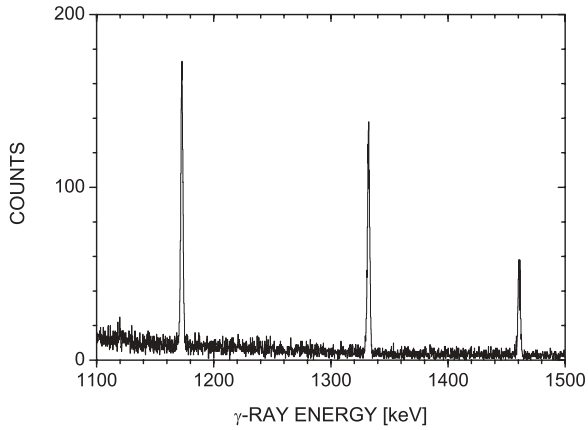


FIG. 2. The $\gamma$-ray spectrum after activation 4 corresponds to the most unfavorable case of the $^{59}$Co$(n, \gamma)^{60}$Co reaction, where the long half-life of $^{60}$Co results in a low signal/background ratio. Nevertheless, the lines at 1173 and 1332 keV could be analyzed with sufficient statistical accuracy. The background peak on the right corresponds to the $^{40}$K line at 1461 keV.

TABLE III. Compilation of systematic uncertainties.

| Source of Uncertainty | Uncertainty (%) | | | | | |
|---|---|---|---|---|---|---|
| | Au | $^{58}$Fe | $^{59}$Co | $^{64}$Ni | $^{63}$Cu | $^{65}$Cu |
| Gold cross section | 1.5 | – | – | – | – | – |
| Number of nuclei | 0.4 | 0.05 | 0.07 | 0.04 | 0.08 | 0.03 |
| Time factors, $f_w$, $f_m$, $f_b$, and $t_{1/2}$ | | | $\leqslant$0.1 | | | |
| Self-absorption, $K_\gamma$ | | | $\leqslant$1.0 | | | |
| Detector efficiency, $\epsilon_\gamma$ | | | 1.5 | | | |
| $\gamma$-Ray intensity per decay, $I_\gamma$ | 0.13 | 3.5 | 0.03 | 0.6 | 2.0 | 1.0 |
| Time integrated neutron flux, $\Phi$ | – | 2.4 | 2.4 | 2.5 | 2.4 | 2.9 |
| Total systematic uncertainty | – | 4.6 | 3.0 | 3.1 | 3.6 | 3.6 |

Since the statistical uncertainties from the activity measurements became practically negligible after averaging the results from repeated activations, the final uncertainties are determined by systematic effects.

### C. Measured cross sections and Maxwellian averages

Table IV shows a summary of the results obtained in all 14 activations together with the corresponding uncertainties. In spite of the variation of the experimental parameters (see Table I), the results are all consistent within the estimated uncertainties, thus confirming the procedures applied in data analysis. These variations included different sample sizes and masses to verify the corrections for finite size and self shielding effects as well as different irradiation times to control uncertainties due to the half-life of the respective product nucleus.

These values represent averaged cross sections for the experimental neutron distribution used in the irradiations. Though the experimental spectrum corresponds in very good approximation to the thermal spectrum for $kT = 25$ keV, the cutoff at 106 keV requires a small correction, in particular if the investigated cross section exhibits a different energy dependence than the gold reference cross section. For the calculation of the final MACSs

$$\langle\sigma\rangle_{kT} = \frac{\langle\sigma v\rangle}{v_T} = \frac{2}{\sqrt{\pi}} \frac{\int_0^\infty \sigma(E_n)\cdot E_n \cdot \exp(-E_n/kT)\cdot dE_n}{\int_0^\infty E_n \cdot \exp(-E_n/kT)\cdot dE_n} \tag{3}$$

this correction was obtained by normalizing the differential $(n,\gamma)$ cross sections, $\sigma_{n,\gamma}(E_n)$, from evaluated data libraries to the new experimental values.

TABLE IV. Activations, $\gamma$-counting, and cross section results[a].

| Reaction | Activation | $\gamma$-Ray energy (keV) | Absorption correction | Cross section (mbarn)[b] | Mean value (mbarn) |
|---|---|---|---|---|---|
| $^{58}$Fe(n,$\gamma$)$^{59}$Fe | 1 | 1099.25 | 0.99 | $12.8 \pm 0.04 \pm 0.6$ | |
| $^{58}$Fe(n,$\gamma$)$^{59}$Fe | 2 | 1099.25 | 0.99 | $12.9 \pm 0.05 \pm 0.6$ | |
| $^{58}$Fe(n,$\gamma$)$^{59}$Fe | 3 | 1099.25 | 0.99 | $13.5 \pm 0.04 \pm 0.7$ | $13.1 \pm 0.6$ |
| $^{59}$Co(n,$\gamma$)$^{60}$Co | 4 | 1173.23 | 1.00 | $40.5 \pm 1.5 \pm 1.2$ | |
| $^{59}$Co(n,$\gamma$)$^{60}$Co | 4 | 1332.49 | 1.00 | $39.6 \pm 1.5 \pm 1.2$ | |
| $^{59}$Co(n,$\gamma$)$^{60}$Co | 5 | 1173.23 | 1.00 | $43.3 \pm 1.1 \pm 1.3$ | |
| $^{59}$Co(n,$\gamma$)$^{60}$Co | 5 | 1332.49 | 1.00 | $40.8 \pm 1.1 \pm 1.3$ | $41.1 \pm 1.5$ |
| $^{64}$Ni(n,$\gamma$)$^{65}$Ni | 6 | 1481.84 | 0.99 | $8.53 \pm 0.03 \pm 0.26$ | |
| $^{64}$Ni(n,$\gamma$)$^{65}$Ni | 7 | 1481.84 | 0.99 | $8.32 \pm 0.03 \pm 0.26$ | |
| $^{64}$Ni(n,$\gamma$)$^{65}$Ni | 8 | 1481.84 | 0.98 | $8.29 \pm 0.4 \pm 0.25$ | $8.40 \pm 0.28$ |
| $^{63}$Cu(n,$\gamma$)$^{64}$Cu | 9 | 1345.77 | 0.99 | $59.2 \pm 0.6 \pm 2.2$ | |
| $^{63}$Cu(n,$\gamma$)$^{64}$Cu | 10 | 1345.77 | 0.99 | $56.9 \pm 2.0 \pm 2.1$ | |
| $^{63}$Cu(n,$\gamma$)$^{64}$Cu | 11 | 1345.77 | 0.99 | $58.2 \pm 2.1 \pm 2.1$ | $58.1 \pm 2.3$ |
| $^{65}$Cu(n,$\gamma$)$^{66}$Cu | 12 | 1039.2 | 0.99 | $30.8 \pm 1.2 \pm 1.1$ | |
| $^{65}$Cu(n,$\gamma$)$^{66}$Cu | 13 | 1039.2 | 0.99 | $31.3 \pm 1.1 \pm 1.1$ | |
| $^{65}$Cu(n,$\gamma$)$^{66}$Cu | 14 | 1039.2 | 0.99 | $28.0 \pm 1.1 \pm 1.0$ | $30.0 \pm 1.3$ |

[a]Cross section averaged over quasi-stellar spectrum.
[b]Statistical and systematic uncertainties listed separately.

TABLE V. Normalization factors $NF$ for the differential cross sections from evaluated data libraries.

| Library | Normalization factors $NF$ | | | | |
|---|---|---|---|---|---|
| | $^{58}$Fe | $^{59}$Co | $^{64}$Ni | $^{63}$Cu | $^{65}$Cu |
| JEFF/3.1 | 0.88 | 1.19 | 0.38 | 0.74 | 0.75 |
| JENDL/3.3 | 0.92 | 1.02 | 0.36 | 0.71 | 0.77 |
| ENDF/VI-8 | 0.67 | 1.19 | 0.38 | 0.74 | 0.75 |

In a first step, the differential cross sections from the online data libraries JEFF/3.1 (www.nea.fr/html/dbdata/JEFF/), JENDL/3.3 (wwwndc.tokai-sc.jaea.go.jp/jendl/), and ENDF/B-VI.8 (www.nndc.bnl.gov/) were folded with the experimental neutron spectrum. Comparison with the measured values yields the normalization factors $NF = \sigma_{exp}/\sigma_{lib}$ listed in Table V. Although the evaluated data, which are all based on the same previous experimental cross sections, exhibit significant discrepancies for $^{64}$Ni, $^{63}$Cu, and $^{65}$Cu as compared to the present data, the resulting correction for transforming the measured value into the MACS at $kT = 25$ keV is fairly small. This is indicated by the differences between the MACS values in Tables VI and VII. Accordingly, the uncertainty of this transformation is negligible compared to the experimental uncertainties, except for the case of $^{59}$Co, where a 2% uncertainty had to be added to the uncertainty of the measured value.

The new results have been used to renormalize the MACSs of Bao *et al.* [9] as indicated in the second lines of Tables VI and VII, respectively. It is conspicuous that the present MACSs are systematically smaller than the previous values of Ref. [9] which are essentially based on TOF measurements performed in the 1970s and early 1980s [15–17]. A possible explanation could be that the background due to sample-scattered neutrons was underestimated in the older TOF experiments. Neutrons scattered in the sample and captured in the detector and/or in surrounding materials produce background, which is difficult to distinguish from true capture events. This background can be as high as 50% for light and medium heavy nuclei [18], where the scattering/capture ratios are large. The correspondingly large and uncertain corrections tend to give rise to large systematic errors.

If the normalization factor $2/\sqrt{\pi}$ [Eq. (3)] is taken into account, the MACSs at $kT = 25$ keV are all in fair agreement with the cross sections measured in the experimental spectrum (Table IV), thus confirming that the experimental neutron spectrum is a very good approximation of the true thermal distribution. Nevertheless, there are non-negligible differences, which reflect the pronounced resonance structure in the cross sections of these medium-mass nuclei.

While the energy dependence of the cross sections has a comparably small effect for the spectrum corrections at $kT = 25$ keV, it becomes a crucial problem for the extrapolation toward lower and higher thermal energies. This can be seen in the lower part of Tables VI and VII, where the energy dependence of evaluated data sets has been used to cover the full range of $s$-process temperatures from $kT = 5$ to 100 keV.

Since it is not obvious, which trend with $kT$ is to be preferred, and since it is beyond the scope of this paper to trace the origin of the differences between various evaluations, the recommended values, which have been used for the

TABLE VI. MACSs of $^{58}$Fe, $^{59}$Co, and $^{64}$Ni compared to the compilation of Bao *et al.* [9].[a]

| | MACS (mbarn) | | | | | | | | | | |
|---|---|---|---|---|---|---|---|---|---|---|---|
| $kT$ (keV) | 5 | 10 | 15 | 20 | 25 | 30 | 40 | 50 | 60 | 80 | 100 |
| | | | | | | $^{58}$Fe$(n,\gamma)^{59}$Fe | | | | | |
| Ref. [9] | 27 | 21 | 17 | 15 | 13 | 12.1±1.3 | 11 | 9.8 | 9.3 | 8.6 | 8.2 |
| Ref. [9][b] | $30^{+9.5}_{-1.4}$ | $23^{+4.6}_{-1.1}$ | $19^{+2.0}_{-0.9}$ | $16.7^{+0.9}_{-0.9}$ | 14.5 ± 0.7 | $13.5^{+0.6}_{-0.8}$ | $12.3^{+0.6}_{-1.5}$ | $10.9^{+0.5}_{-1.4}$ | $10.4^{+0.5}_{-1.9}$ | $9.6^{+0.5}_{-2.7}$ | $9.1^{+0.4}_{-3.3}$ |
| JEFF | 30.7 | 23.6 | 19.0 | 16.3 | 14.5 ± 0.7 | 13.3 | 11.6 | 10.5 | 9.63 | 8.37 | 7.48 |
| JENDL | 39.5 | 27.9 | 20.8 | 17.0 | 14.6 ± 0.7 | 13.0 | 10.9 | 9.55 | 8.58 | 7.26 | 6.39 |
| ENDF | 32.8 | 24.2 | 19.1 | 16.3 | 14.5 ± 0.7 | 13.2 | 11.3 | 9.90 | 8.73 | 6.98 | 5.84 |
| | | | | | | $^{59}$Co$(n,\gamma)^{60}$Co | | | | | |
| Ref. [9] | 110 | 82 | 63 | 52 | 44 | 38±4 | 32 | 27 | 22 | 12 | 8 |
| Ref. [9][b] | $115^{+77}_{-7}$ | $85.4^{+17}_{-5}$ | $65.6^{+6.6}_{-3.9}$ | $54.1^{+3.4}_{-3.3}$ | 45.8 ± 2.7 | $39.6^{+2.7}_{-2.5}$ | $33.3^{+2.1}_{-2.5}$ | $28.1^{+2.3}_{-1.8}$ | $22.9^{+4.2}_{-1.4}$ | $12.5^{+10.5}_{-0.7}$ | $8.3^{+12.1}_{-0.5}$ |
| JEFF | 192 | 102 | 71.0 | 55.7 | 46.7 ± 1.7 | 40.9 | 33.9 | 29.7 | 26.8 | 22.9 | 20.4 |
| JENDL | 177 | 97.0 | 68.1 | 53.1 | 44.3 ± 1.6 | 38.7 | 31.7 | 27.5 | 24.7 | 20.9 | 18.5 |
| ENDF | 192 | 102 | 70.7 | 55.3 | 46.4 ± 1.7 | 40.8 | 33.9 | 29.7 | 26.9 | 23.0 | 20.4 |
| | | | | | | $^{64}$Ni$(n,\gamma)^{65}$Ni | | | | | |
| Ref. [9] | 12.8 | 14.8 | 13.1 | 11.2 | 9.8 | 8.7±0.9 | 7.4 | 6.6 | 6.1 | 5.5 | 5.2 |
| Ref. [9][b] | $11.8^{+16}_{-2.1}$ | $13.6^{+8.6}_{-2.6}$ | $12.0^{+3.8}_{-1.6}$ | $10.3^{+1.4}_{-0.7}$ | 9.0 ± 0.3 | $8.0^{+0.5}_{-0.8}$ | $6.8^{+0.8}_{-1.7}$ | $6.1^{+0.5}_{-2.2}$ | $5.6^{+0.4}_{-2.4}$ | $5.1^{+0.17}_{-2.6}$ | $4.8^{+0.16}_{-2.7}$ |
| JEFF | 9.7 | 11.0 | 10.5 | 9.7 | 9.0 ± 0.3 | 8.4 | 7.3 | 6.5 | 5.9 | 5.1 | 4.5 |
| JENDL | 27.8 | 22.2 | 15.8 | 11.7 | 9.0 ± 0.3 | 7.2 | 5.1 | 3.9 | 3.2 | 2.5 | 2.1 |
| ENDF | 9.7 | 11.0 | 10.5 | 9.7 | 9.0 ± 0.3 | 8.4 | 7.6 | 6.6 | 6.0 | 5.1 | 4.5 |

[a]For comparison with measured cross section values in table IV multiply with $\sqrt{\pi}/2$

[b]Normalized to the measured value.

TABLE VII. MACSs of $^{63}$Cu, and $^{65}$Cu compared to the compilation of Bao *et al.* [9].[a]

| | MACS (mbarn) | | | | | | | | | | |
|---|---|---|---|---|---|---|---|---|---|---|---|
| $kT$ (keV) | 5 | 10 | 15 | 20 | 25 | 30 | 40 | 50 | 60 | 80 | 100 |
| | | | | | | $^{63}$Cu$(n,\gamma)^{64}$Cu | | | | | |
| Ref. [9] | 331 | 182 | 136 | 114 | 102 | 94±10 | 83 | 79 | 76 | 66 | 58 |
| Ref. [9][b] | $198^{+22}_{-8}$ | $109^{+18}_{-4.4}$ | $81^{+11}_{-3.2}$ | $68^{+5.4}_{-2.7}$ | $60.3 \pm 2.4$ | $56^{+2.2}_{-5.2}$ | $50^{+2.0}_{-7.9}$ | $47^{+1.9}_{-10}$ | $45^{+1.8}_{-12}$ | $39^{+1.6}_{-10}$ | $35^{+1.4}_{-9.6}$ |
| JEFF | 219 | 126 | 91.6 | 72.7 | $61.0 \pm 2.4$ | 53.1 | 43.4 | 37.5 | 33.6 | 28.7 | 25.5 |
| JENDL | 201 | 120 | 88.0 | 71.2 | $61.1 \pm 2.4$ | 54.2 | 45.3 | 39.7 | 35.7 | 30.3 | 26.7 |
| ENDF | 210 | 126 | 90.2 | 71.5 | $58.8 \pm 2.3$ | 51.3 | 42.4 | 37.1 | 33.6 | 28.7 | 25.5 |
| | | | | | | $^{65}$Cu$(n,\gamma)^{66}$Cu | | | | | |
| Ref. [9] | 152 | 79 | 58 | 49 | 44 | 41±5 | 37 | 33 | 31 | 27 | 25 |
| Ref. [9][b] | $111^{+4.9}_{-21}$ | $57^{+2.6}_{-2.6}$ | $42^{+2.7}_{-1.8}$ | $36^{+1.7}_{-1.6}$ | $32 \pm 1.4$ | $30^{+1.3}_{-1.9}$ | $27^{+1.2}_{-3.2}$ | $24^{+1.1}_{-3.2}$ | $23^{+1.0}_{-4.3}$ | $20^{+0.9}_{-4.2}$ | $18^{+0.8}_{-4.1}$ |
| JEFF | 90.1 | 56.7 | 43.7 | 36.7 | $32.4 \pm 1.4$ | 29.3 | 25.2 | 22.4 | 20.3 | 17.4 | 15.3 |
| JENDL | 92.9 | 57.5 | 44.0 | 36.7 | $32.0 \pm 1.4$ | 28.6 | 24.0 | 21.0 | 18.8 | 15.9 | 14.0 |
| ENDF | 90.2 | 56.5 | 43.2 | 36.0 | $31.6 \pm 1.4$ | 28.7 | 25.0 | 22.5 | 20.5 | 17.5 | 15.4 |

[a]For comparison with measured cross section values in Table IV multiply with $\sqrt{\pi}/2$
[b]Normalized to the measured value.

$s$-process calculations discussed in the following section, were extrapolated following the Bao *et al.* compilation [9]. This choice was motivated by the fact that these data include the most recent TOF data available.

The uncertainties of the extrapolated MACSs were estimated by comparison with the upper and lower bounds obtained by using the evaluated cross sections from the data libraries. The uncertainties of the recommended values are, therefore, composed of the experimental uncertainties originating from the measured data and of the contributions defined by the differences with respect to the values in lines 3 to 5 of Tables VI and VII.

In concluding this section two points are worth noting. (i) Among the MACSs listed in Tables VI and VII, those from the compilation of Bao *et al.* [9] agree best with the cross sections reported here. This is plausible because this compilation represents a comprehensive update on the basis of recent cross section results, whereas the evaluated data libraries are mostly focused on data for technologically relevant materials and are less frequently revised in other cases. Therefore, it is important to maintain a comprehensive library dedicated to nuclear cross sections for the rapidly developing field of nuclear astrophysics, as it is provided by the KADONIS project (http://nuclear-astrophysics.fzk.de/kadonis), an online extension of the Bao *et al.* compilation. (ii) The extrapolation to lower and higher thermal energies implies still rather large uncertainties, particularly for the MACS of $^{64}$Ni, which exhibits the largest discrepancies at lower values of $kT$. To solve this pending problem, it is mandatory to perform improved TOF measurements using state of the art detection and analysis techniques.

## IV. ASTROPHYSICAL IMPLICATIONS

### A. Stellar models

The weak $s$ process, which produces most of the $s$-process abundances between the iron peak and strontium (e.g., Ref. [5]), takes place during the presupernova evolution of massive stars with $M \geqslant 8M_{\odot}$. Neutrons are mainly provided by the $^{22}$Ne$(\alpha,n)^{25}$Mg reaction during convective core He burning and during convective shell C burning. One has to consider that also $^{13}$C$(\alpha,n)^{16}$O and $^{17}$O$(\alpha,n)^{20}$Ne reactions contribute to a minor extent, recycling neutrons previously captured by the abundant $^{12}$C and $^{16}$O.

The $s$ process during the core He burning phase [19–21] depends on the initial metallicity of the star, so that it behaves as a secondary nucleosynthesis process. $^{22}$Ne is produced by double $\alpha$ capture on $^{14}$N, which in turn results from conversion of the initial CNO abundances during the previous H burning. In the early phases of convective core He burning, $^{14}$N is fully converted to $^{18}$O via $^{14}$N$(\alpha,\gamma)^{18}$F$(\beta^{+}\nu)^{18}$O. Later on, when $^{4}$He has been depleted to about 10% in mass fraction and the central temperature has increased up to $T_8 \approx 2.5$, $^{22}$Ne is produced by further $\alpha$ captures on $^{18}$O. The $^{22}$Ne$(\alpha,n)^{25}$Mg reaction becomes an efficient neutron source only in the last phases of core He burning, close to He exhaustion, when central temperatures of $T_8 = 3$–$3.5$ are reached [21].

Most of the products of core He burning are subsequently exposed to a second neutron irradiation during the convective shell C burning phase, when temperatures of $10^9$ K and densities of $10^5$ g/cm$^3$ are reached at the bottom of the shell. In the $25M_{\odot}$ model used for the present discussion, the outer convective shell extends during C burning from about $2M_{\odot}$ up to about $6M_{\odot}$, close to the maximum extension of the previous convective He burning core. While the abundances in the inner zone up to about $3.5M_{\odot}$ are modified in the final supernova explosion, in particularly destroying by photodisintegration all previously produced $s$-process abundances, the $s$-process material in the outer zones of the C burning shell are ejected essentially unchanged [2,3]. Carbon burns via the reaction channels $^{12}$C$(^{12}$C, $\alpha)^{20}$Ne and $^{12}$C$(^{12}$C, $p)^{23}$Na, thus providing the $\alpha$ particles for $^{22}$Ne$(\alpha,n)^{25}$Mg reactions on the $^{22}$Ne, left behind at previous core He exhaustion, as well as the protons for the activation of the proton capture channels.

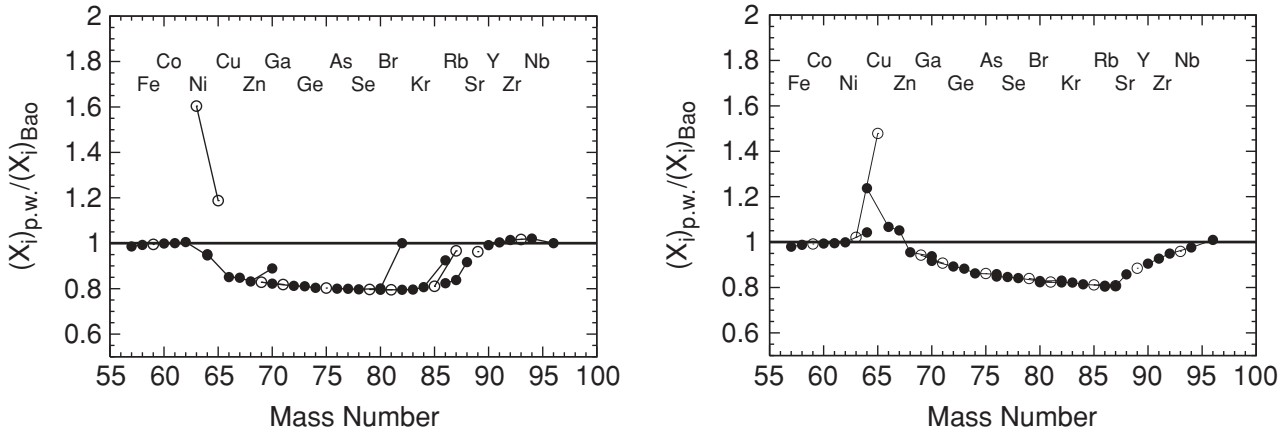


FIG. 3. Nucleosynthesis yields of stellar model calculations for a 25 $M_\odot$ star at the end of the core helium burning phase (left) and carbon burning phase (right) with the new $^{63,65}$Cu cross sections relative to the yields obtained with the previous cross sections (p.w. stands for present work and Bao for Ref. [9], even and odd Z elements are distinguished by black and open symbols, respectively).

A first study of C burning nucleosynthesis for the light isotopes [22] was complemented in Ref. [4] by a detailed discussion of the concomitant *s*-process nucleosynthesis during this phase, which in a convective shell is characterized by a short time scale of the order of 1 yr and by a high neutron density. These results were confirmed by full network calculations for stellar evolution up to the supernova explosion [2,3,6,23,24].

### B. Implications of the present MACS

To explore the effect for the weak *s* process, stellar model calculations for a 25 $M_\odot$ star were performed with an updated post-processing code described in Refs. [4,21,25].

The effect of the new Cu cross sections is illustrated in Fig. 3. The nucleosynthesis yields at the end of core He burning and of shell C burning are plotted relative to the yields obtained with the previous cross sections. The strong impact of individual $(n, \gamma)$ cross sections that has already been found for the case of $^{62}$Ni [26], has now also been confirmed by the new Cu cross sections. The propagation wave due to the new MACSs of Cu ends essentially at Rb, but a small effect can still be seen up to Nb.

The differences resulting from the cross sections reported here refer mostly to the effect of the branchings in the reaction path. During core He burning, practically all potential branchings are inactive because of the low neutron density. Neutron-rich isotopes such as $^{70}$Zn, $^{76}$Ge, $^{81}$Br, $^{82}$Se, and $^{87}$Rb are not reached by the reaction flow and are, therefore, less influenced by the reduced *s*-process efficiency. At the much higher fluxes and temperatures during shell C burning these branchings are strongly activated; this implies that even $^{70}$Zn, $^{76}$Ge, and $^{82}$Se, which are commonly considered as *r*-only nuclei, are affected by the propagation wave as much as the other isotopes.

Consequently, reliable abundance predictions for the weak *s* process can only be made if the stellar neutron capture cross sections of *all* involved isotopes are known with high accuracy at He and C burning temperatures ($kT \sim 30$ and $\sim 90$ keV, respectively).

In the set of cross sections studied, the new values of the Cu isotopes showed the largest impact. Compared to the previously recommended values [9] the new MACSs of $^{63}$Cu and $^{65}$Cu at 30 keV are smaller by 70% and 40%, respectively. In this case, the propagation effect obtained in the stellar model calculations is visible over the entire distribution up to $A = 95$.

At the end of core He burning, the $^{63}$Cu abundance increases according to the decrease of the MACS, but the abundance of $^{65}$Cu develops in a more complex way. The reason is that under He burning conditions $^{65}$Cu is produced via two paths, i.e., via $^{63}$Cu$(n, \gamma)^{64}$Cu$(\beta^+)^{64}$Ni$(n, \gamma)^{65}$Ni$(\beta^-)^{65}$Cu and via $^{63}$Cu$(n, \gamma)^{64}$Cu$(\beta^-)^{64}$Zn$(n, \gamma)^{65}$Zn$(\beta^+)^{65}$Cu. In both cases, a smaller $^{63}$Cu cross section leads to a reduced production of $^{65}$Cu and thus works against the effect of the smaller MACS of $^{65}$Cu itself. The propagation wave triggered by the smaller Cu cross sections is reaching up to Zr. This implies a reduction in the average *s*-process efficiency between Zn and Sr by 20% with respect to the calculation based on the previous MACSs for $^{63}$Cu and $^{65}$Cu [9]. The propagation wave stops at the Sr-Y-Zr peak because of the low neutron exposure of the weak *s* process.

By the end of shell C burning most of the initial $^{63}$Cu is depleted by neutron captures, because the $(n, \gamma)$ channel is favored at the branch point $^{63}$Ni with respect to the $(\beta^-)$ channel (Fig. 4). The final $^{63}$Cu abundance is mainly of

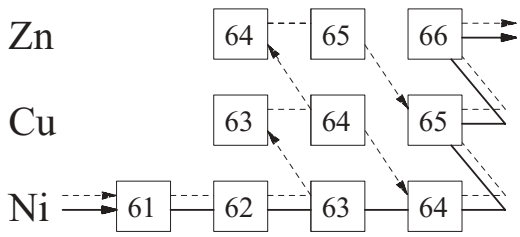


FIG. 4. The *s*-process path in the vicinity of Cu. The main reaction flows during core-He burning and shell-C burning are indicated by dashed and solid lines, respectively.

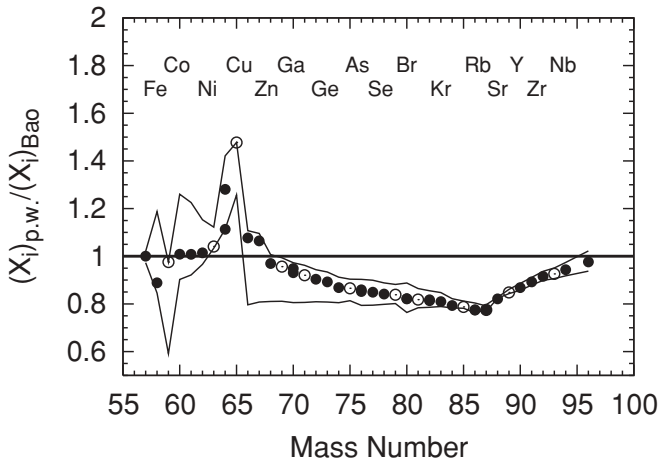


FIG. 5. Nucleosynthesis yields between Fe and Nb illustrating the final *s*-process yields after shell C burning for a 25 $M_\odot$ star with [Fe/H] = 0. To illustrate the combined effect of all new cross sections the yield is plotted relative to the standard case using the cross sections of [9] (p.w. stands for present work and Bao for Ref. [9], even and odd Z elements are distinguished by black and open symbols, respectively). The thin lines correspond to the upper and lower limits of the cross sections in Tables VI and VII and demonstrate the uncertainties stemming from the extrapolation of the measured cross sections to higher and lower energies.

radiogenic origin due to the decay of $^{63}$Ni, and for this reason the new MACS of $^{63}$Cu is of minor importance in this respect. On the other hand, the $^{65}$Cu abundance is higher because of the higher initial abundance after core He burning and also because of the smaller new MACS. The abundance of $^{64}$Zn reflects the higher initial $^{63}$Cu value, because it is produced via $^{63}$Cu$(n,\gamma)^{64}$Cu$(\beta^-)^{64}$Zn. Nevertheless, the initial abundance of $^{64}$Zn is significantly reduced during shell C burning because the $(n,\gamma)$ channel is favored at $^{63}$Ni (Fig. 4). In general, the 20% decrease of the *s*-process efficiency between Zn and Sr observed at the end of the previous core He burning is maintained during the shell C burning phase.

The combined effect of all new cross sections reported here on the abundance distribution of the weak *s* process is shown in Fig. 5 for the situation after the final shell C burning compared to the results obtained with the previous cross section of Ref. [9]. The reduction in *s*-process efficiency due to the smaller stellar cross sections of the nuclei close to the Fe group (determined in this work) is clearly visible by the significant 20% decrease in the abundances between Zn and Sr.

The range of uncertainties, which are caused by the extrapolation from the measured energy at $kT = 25$ keV to the higher energies around $kT = 90$ keV during shell C burning, are indicated by the thin lines in Fig. 5. To improve this situation, complementary TOF measurements are clearly needed in the mass region $56 \leqslant A \leqslant 70$.

With respect to the *r*-residual method it is important to note that after shell C burning the reduction in *s*-process efficiency toward the region of heavier isotopes is more pronounced than after core He burning, and extends even into the mass region beyond the neutron magic nuclei with $N = 50$.

## V. CONCLUSIONS

The present measurements have shown that the nucleosynthesis yields for the weak *s* process, calculated with stellar models for massive stars, still show large variations due to the uncertainties of the involved neutron capture cross sections. Unlike the main s process, flow equilibrium is not reached during the weak *s* process. Therefore, improved neutron capture cross sections do not only influence the yield of the respective isotope, but also the production of all heavier nuclei on the weak *s*-process path.

The present activation measurements at $kT = 25$ keV have provided a set of significantly improved MACSs for $^{58}$Fe, $^{59}$Co, $^{64}$Ni, $^{63}$Cu, and $^{65}$Cu. These results were shown to cause a significant propagation effect in the abundance predictions for the weak *s* process component, resulting in a 20% lower *s*-process efficiency between Zn and Sr. In fact, the propagation wave up to Sr is mainly due to the new cross sections of $^{63}$Cu and $^{65}$Cu. These findings strongly emphasize that reliable stellar $(n,\gamma)$ cross sections for the abundant nuclei near the Fe seed are crucial for quantitative *s*-process calculations in massive stars [33]. The extrapolation of the present results to the higher temperatures of shell-C burning remains problematic, however, because of the pronounced resonance structure of these cross sections. Therefore, complementary TOF measurements with state of the art techniques are urgently called for. This is also true for a large number of light neutron poisons, which have a strong impact on the overall neutron balance as well.

## ACKNOWLEDGMENTS

We are thankful to D. Roller, E.-P. Knaetsch, and W. Seith for their support during the measurements. M. P. and R. G. acknowledge support by the Italian MIUR-PRIN06 Project "Late phases of Stellar Evolution: Nucleosynthesis in Supernovae, AGB stars, Planetary Nebulae".

[1] O. Straniero, R. Gallino, M. Busso, A. Chieffi, C. Raiteri, M. Limongi, and M. Salaris, Astrophys. J. **440**, L85 (1995).
[2] A. Heger, Technical Report, http://www.ucolick.org/~alex/ (2006).
[3] M. Limongi, Technical Report, http://www.mporzio.astro.it/~limongi/ (2006).
[4] C. Raiteri, M. Busso, R. Gallino, and G. Picchio, Astrophys. J. **371**, 665 (1991).
[5] C. Raiteri, R. Gallino, M. Busso, D. Neuberger, and F. Käppeler, Astrophys. J. **419**, 207 (1993).
[6] M. Limongi, O. Straniero, and A. Chieffi, Astrophys. J. Suppl. **129**, 625 (2000).
[7] T. Rauscher, A. Heger, R. Hoffman, and S. Woosley, Astrophys. J. **576**, 323 (2002).
[8] K.-L. Kratz, K. Farouqi, B. Pfeiffer, J. W. Truran, C. Sneden, and J. J. Cowan, Astrophys. J. **662**, 39 (2007).

[9] Z. Bao, H. Beer, F. Käppeler, F. Voss, K. Wisshak, and T. Rauscher, At. Data Nucl. Data Tables **76**, 70 (2000).
[10] H. Beer and F. Käppeler, Phys. Rev. C **21**, 534 (1980).
[11] N. Patronis, P. Assimakopoulos, D. Karamanis, S. Dababneh, M. Heil, F. Käppeler, R. Plag, P. Koehler, A. Mengoni, R. Gallino *et al*., Phys. Rev. C **69**, 025803 (2004).
[12] S. O'Brien, S. Dababneh, M. Heil, F. Käppeler, R. Plag, R. Reifarth, R. Gallino, and M. Pignatari, Phys. Rev. C **68**, 035801 (2003).
[13] U. Ratzel, C. Arlandini, F. Käppeler, A. Couture, M. Wiescher, R. Reifarth, R. Gallino, A. Mengoni, and C. Travaglio, Phys. Rev. C **70**, 065803 (2004).
[14] W. Ratynski and F. Käppeler, Phys. Rev. C **37**, 595 (1988).
[15] M. J. Kenny, B. J. Allen, and R. L. Macklin, Aust. J. Phys. **30**, 605 (1977).
[16] R. L. Macklin, Nucl. Sci. Eng. **88**, 129 (1984).
[17] A. R. de L. Musgrove, B. Allen, and R. Macklin, J. Phys. G **4**, 771 (1978).
[18] A. R. de L. Musgrove, B. Allen, and R. Macklin, *Neutron Physics and Nuclear Data for Reactors and other Applied Purposes* (OECD Nuclear Energy Agency, Paris, 1978), p. 426.
[19] S. Lamb, W. Howard, J. Truran, and I. Iben, Astrophys. J. **217**, 213 (1977).
[20] N. Prantzos, M. Arnould, and J.-P. Arcoragi, Astrophys. J. **315**, 209 (1987).
[21] C. Raiteri, M. Busso, R. Gallino, G. Picchio, and L. Pulone, Astrophys. J. **367**, 228 (1991).
[22] W. Arnett and J. Truran, Astrophys. J. **157**, 339 (1969).
[23] S. Woosley, A. Heger, and T. Weaver, Rev. Mod. Phys. **74**, 1015 (2002).
[24] L.-S. The, M. F. El Eid, and B. S. Meyer, Astrophys. J. **655**, 1058 (2007).
[25] M. Pignatari, R. Gallino, C. Baldovin, M. Wiescher, F. Herwig, A. Heger, M. Heil, and F. Käppeler, PoS (NIC-IX) **061**, (2006).
[26] H. Nassar, M. Paul, I. Ahmad, D. Berkovits, M. Bettan, P. Collon, S. Dababneh, S. Ghelberg, J. Greene, A. Heger *et al*., Phys. Rev. Lett. **94**, 092504 (2005).
[27] C. Baglin, Nucl. Data Sheets **95**, 215 (2002).
[28] J. Tuli, Nucl. Data Sheets **100**, 347 (2003).
[29] M. Bhat, Nucl. Data Sheets **69**, 209 (1993).
[30] B. Singh, Nucl. Data Sheets **78**, 395 (1996).
[31] M. Bhat, Nucl. Data Sheets **83**, 789 (1998).
[32] Z. Chunmei, Nucl. Data Sheets **95**, 59 (2002).
[33] M. Pignatari, R. Gallino, C. Baldovin, and F. Herwig, in *From Lithium to Uranium: Elemental Tracers of Early Cosmic Evolution, IAU Symposium 228*, edited by V. Hill, P. François, and F. Primas (Cambridge University Press, Cambridge, 2005) p. 495.